Journal of Inorganic and General Chemistry
ZAAC
Zeitschrift für anorganische und allgemeine Chemie
DOI: 10.1002/zaac.201800122
ARTICLE

Structure, Bonding, Reactivity and Spectral Features of Putative Ni^{III}=O Species: A Theoretical Perspective

Bhawana Pandey,[a] Kallol Ray,*[b] and Gopalan Rajaraman*[a]

Dedicated to Prof. Peter Comba on the Occasion of his 65th Birthday

Abstract. Although extensive efforts have been undertaken to study in detail the formation, reactivity, and stability of mononuclear Ni^{III} species bearing a terminal oxo/hydroxo group, electronic structure of such high-valent species is not unambiguously established. Using a combination of density functional and ab initio CASSCF methods, we have probed the structure, bonding, spectral features, and reactivity of putative Ni^{III}-oxo/hydroxo complexes supported by a tetradentatetripodal TMG_3tren {tris[2-(*N*-tetramethylguanidyl)ethyl]amine} ligand. Our main focus is to establish the structure and bonding of putative Ni^{III}=O/Ni^{III}–OH/Ni^{IV}=O species and explore the mechanism by which such species can be plausibly generated from an acylperoxonickel(II) intermediate. The characteristic spectral features of these species are computed and compared to available experimental data to obtain confidence on the computed data. In addition, we have explored the reactivity of the Ni^{III}=O species in intra- and inter- molecular C–H bond activation reactions. Our results reveal that these species are extremely reactive and possess a significant oxyl radical character, which is the driving force behind its potent reactivity.

Introduction

Transition metal ions play a critical role in various oxidation and electron transfer processes that occur in nature as well as in industry and academics.[1] The high valent metal-oxo or hydroxo groups also participate in a series of electron transfer processes in biological and chemical transformations. Because of their wide biological and chemical significance, an immediate issue is to understand the reactivity differences among these related active transition metal ion species. Iron,[2] manganese,[3] and copper[4] ions containing metalloenzymes are very popular but the role of other metal ions are also remarkably important. Study of these complexes help us to better understand the detailed mechanism of the reactions catalysed by metalloenzymes and offer clues for the development of efficient biomimetic catalyst.

Moreover, the study of nickel complexes is very essential in metalloenzyme chemistry[5] due to their involvement in various biological reactions and in homogeneous catalysis.[6] Nickel enzymes play important roles in global biological carbon, nitrogen, and oxygen cycle. Hydrogenases,[7] Ni-SOD,[8] urease,[9] glyoxalase,[10] CO dehydrogenase,[11] etc. are few examples of metalloenzymes containing nickel ion in their active sites. The Ni^{III} oxidation state is very unusual for nickel chemistry because the synthesis and characterization of stable Ni^{III} complexes are challenging.[12,13] Nevertheless, over the last few years, the study of high-valent central Ni ions are gaining great attention because of their proposed involvement in a variety of Ni-based oxidation reactions.[14,15] These complexes are very rare, as they have transient properties at room temperature, and correspondingly, only a few of them have been successfully characterized.[16] *Itoh* et al. have reported a nickel(II) complex $[Ni(TPA)(OAc)(H_2O)](BPh_4)$, as a very efficient and selective catalyst, for alkane hydroxylation with *m*-chloroperbenzoic acid (*m*-CPBA) as an oxidant.[14c] This has been extended later to include Ni^{II} complexes with different ligand architecture suggesting the formation of highly reactive [Ni^{III}=O] species as the active intermediates in these reactions.[17] Furthermore, based on the experimental and theoretical studies, Ni^{III}=O species has also been reported as a most potent oxidant for the conversion of methane to methanol.[18] However, identification of Ni^{III}=O species under catalytic turnover conditions has not been achieved, which makes the mechanism of Ni^{II}/mCPBA mediated oxidation reactions ambiguous.

Previously, the stable oxo or superoxo complexes of Fe, Co, and Cu complexes[13,19] with a tetradentatetripodal TMG_3tren ligand {tris[2-(*N*-tetramethylguanidyl)ethyl] amine} have been reported, and recently *Ray* et al. have synthesized a mononuclear Ni^{II} complex, $[Ni^{II}(TMG_3tren)]^{2+}$, with the same ligand.[20] Further exploration of the reactivity of the $[Ni^{II}(TMG_3tren)]^{2+}$ complex with *m*-CPBA reveal the formation of a very rare nickel(III)-oxygen species and kinetic and spectroscopic studies have been performed to confirm the generation of Ni^{III}-oxygen species. The proposed mechanism involves coordination of Ni^{II} to the *meta*-chloroperbenzoate

* Dr. K. Ray
E-Mail: kallol.ray@chemie.hu-berlin.de
* Dr. G. Rajaraman
E-Mail: rajaraman@chem.iitb.ac.in
[a] Department of Chemistry
Indian Institute of Technology Bombay
400 076, Powai, India
[b] Institut fár Chemie
Humboldt-Universität zu Berlin
Brook-Taylor-Straße 2
12489 Berlin, Germany
Supporting information for this article is available on the WWW under **http://dx.doi.org/10.1002/zaac.201800122** or from the author.

anion followed by the homolytic cleavage of O–O bond of the acylperoxoNi^{II} complex.[14b,17,21] This generates a highly reactive Ni^{III}=O intermediate. Despite extensive experimental studies for the formation of mononuclear Ni^{III} species bearing a terminal oxo/hydroxo group, a detailed theoretical study focusing on the formation, stability, bonding and reactivity is lacking and is very essential to completely understand the oxidizing potential of this species.

Herein, we aim to explore the mechanism for the generation of Ni^{III}-oxo/hydroxo complexes with a tetradentatetripodal TMG_3tren ligand by using DFT methods. We try to answer the following intriguing questions: (i) what is the exact mechanism, by which the Ni-oxo species is generated and what are their kinetic barriers?, (ii) the Ni^{II}–O$^{\bullet}$ and Ni^{III}=O species are isoelectronic. Which are the stable species here and what are the differences in bonding between these two electromeric structures?, and (iii) how efficient is this Ni-oxo species towards C–H bond activation (both intra and inter)?

Results and Discussion

The reaction starts with the formation of [Ni^{II}(TMG_3tren)(OTf)]$^+$ (**1**), which upon oxidation with *meta*-chloroperbenzoic acid (*m*-CPBA) forms the acylperoxonickel(II) complex (**2**) (see Scheme S1 Supporting Information). The next steps involve the cleavage of the O···O bond of complex **2** either via homolysis or heterolysis, leading to the generation of high-valent Ni^{III}=O/OH or Ni^{IV}=O/OH species, respectively. The proposed mechanism adapted for DFT calculations is shown in Scheme 1. There are two possible spin states for the complex **1** viz. S = 1 (^{3}**1**) and S = 0 (^{1}**1**). Our calculations reveal triplet state (^{3}**1**) as the ground state with the singlet state estimated to be 113.0 kJ·mol^{-1} higher in energy. In CH_2Cl_2 solution an effective magnetic moment of 2.95 BM was determined at 25 °C, consistent with the S = 1 ground state of **1**. The optimized structure of ^{3}**1** shows a trigonal bipyramidal (TBP) arrangement around the central metal atom with the calculated Ni–N_{ax} and Ni–O bond lengths of 2.197 Å (X-ray 2.116 Å[20]) and 2.066 Å (X-ray 2.103 Å[20]), respectively (Figure 1).

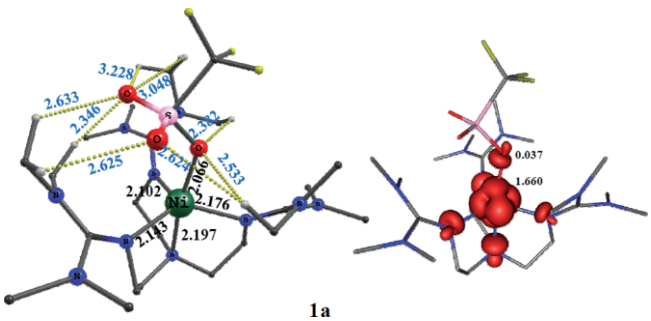

Figure 1. B3LYP optimized structures and spin density plots of the ground state of **1**.

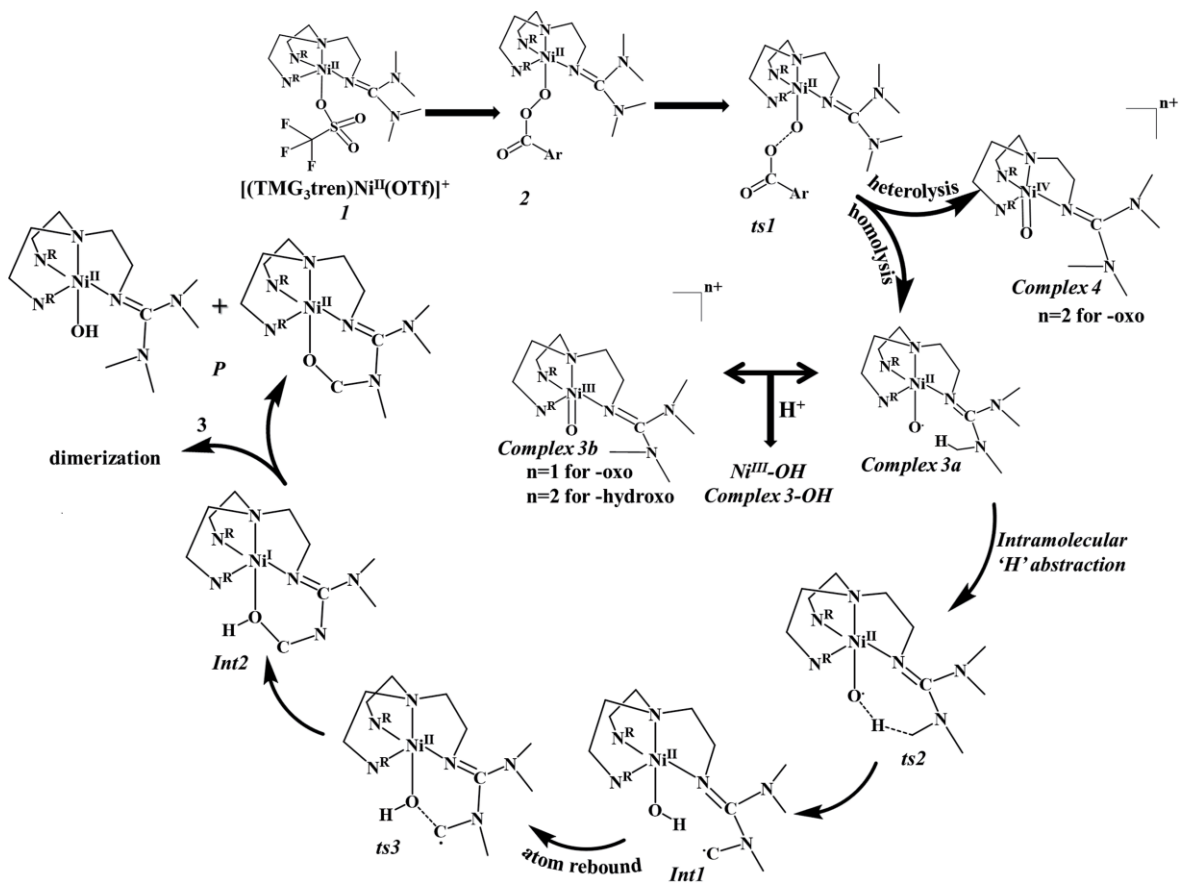

Scheme 1. Schematic representation of the proposed mechanism for the formation and self-decay of complex **3**.

From Figure 1, it is clear that the oxygen atoms of the triflate (–OTf) moiety has several C–H···O interactions with the methyl hydrogen atoms present in the vicinity at the distance ranging from ca. 2.3 Å to 3.4 Å (see Figure 1). The nitrogen atoms of the TMG_3tren ligand also interact with the nearby hydrogen atoms; the combined hydrogen bonding interactions contribute to the overall stability of ^{3}**1** in the high spin state. These structural parameters are in agreement with the experiments (see Table S2, Supporting Information). The calculation reveals a $(d_{xz})^2(d_{yz})^2(d_{xy})^2(d_{x^2-y^2})^1(d_{z^2})^1$ electronic configuration with the d_{xz}/d_{yz} and $d_{xy}/d_{x^2-y^2}$ orbitals being nearly degenerate. The near degeneracy of the d_{xy} and $d_{x^2-y^2}$ orbitals lead to a Jahn-Teller distortion and this causes the Ni–N distances in the equatorial plane to be asymmetric. As predicted by us earlier, this arrangement is expected to also possess a very large negative zero-field splitting parameter.[22] Experimental determination of the zero-field splitting is underway in our laboratory and will be reported in a subsequent publication. The spin density on Ni (ρNi) atom is found to be 1.660 and this indicates a strong delocalization of spin densities to the ligand atoms.

Formation of species **2** from species **1** is expected via a dissociative pathway. Our calculations indicate that the formation of a four coordinate intermediate $[Ni^{II}(TMG_3tren)]^{2+}$ (for the optimized structure see Figure S4, Supporting Information) from **1** is exothermic by 25 kJ·mol^{-1} and addition of *m*-CPBA to species **1** is energetically favorable by –59.8 kJ·mol^{-1} (see Figure 2). Accordingly, the formation of **2** from **1** is an energetically facile process.

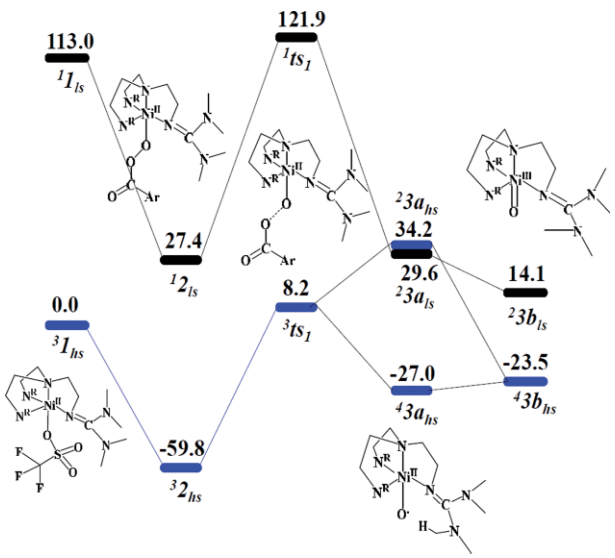

Figure 2. B3LYP computed energy profile diagram for the formation of complex **3a** and **3b** from complex **1**.

The optimized structure of the S = 1 state of species **2** (^{3}**2**$_{hs}$) is shown in Figure 3 along with the corresponding spin density plot. Although, **2** was found to be a transient intermediate experimentally, acylperoxo Ni^{II} complexes have often been characterized[23] and proposed as a reactive intermediate in a variety of Ni^{II} catalysed oxidation reactions. In contrast to complex **1**, the Ni–N_{ax} bond length is predicted to be slightly longer in complex **2**. The O···O bond length is found to be 1.460 Å, which comes in the range for peroxide O–O bond lengths [24] confirming the acylperoxo nature of complex **2**. In the triplet state, the spin density value on Ni^{II} ion is found to be 1.641. The spin density is delocalized into the coordinated N/O atoms. While the proximal oxygen atom possesses significant spin density compared to the other atoms, the distal oxygen exhibits small negative spin density. The triplet-singlet gap is found to decrease to 87.3 kJ·mol^{-1} for complex **2** from 113 kJ·mol^{-1} in **1**. We have also explored the possibility for the formation of Ni^{III}-acylperoxo species (**2′**). The optimized structure and spin density plot is shown in Figure 3. The ^{3}**2′** state is found to be higher in energy by 192 kJ·mol^{-1} and suggest that this is energetically not feasible.

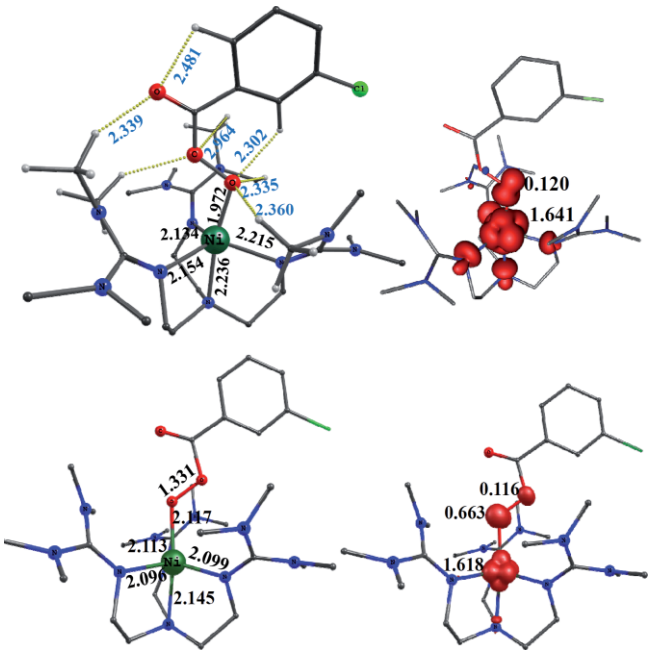

Figure 3. B3LYP optimized structures and spin density plots of the ground state of **2** and **2′**.

In the next step, the O···O bond cleavage either via homolysis or by heterolysis is expected via **ts1**. Homolysis will generate a Ni^{III}=O species, while heterolysis will lead to the formation of a Ni^{IV}=O species (see Scheme 1). The optimized structure of ^{3}**ts1** is shown in Figure 4 along with the corresponding spin density plot. At the transition state, the O···O bond length

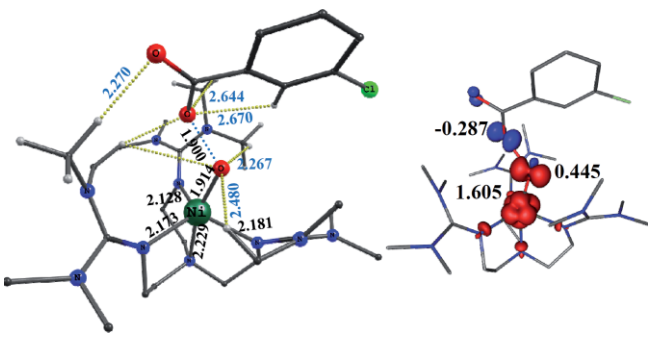

Figure 4. B3LYP optimized structures and spin density plots of the ground state for the O···O bond breaking step (^{3}**ts1**).

is found to increase from 1.460 Å to 1.900 Å, confirming a cleavage of this bond at the transition state itself (late transition state) and at the same time a significant shortening of the Ni–O bond is found (shortened by 0.058 Å compared to **2**).

The estimated barrier height is found to be 68.0 kJ·mol^{-1} at the triplet surface (Figure 2) from species **2**. Thus in contrast to other stable metal-acylperoxo species,[25] the O···O bond cleavage step in **2** is thermodynamically favorable. Notably, at the singlet surface the barrier is estimated to be much larger (94.5 kJ·mol^{-1} from ^{1}**2** species), which may suggest an exclusive cleavage of the O···O bond at the triplet surface. The spin density values on Ni, O1 (proximal), and O2 (distal) are found to be 1.605, 0.445, and –0.287, respectively. Significant spin densities at the oxygen atoms reveal that the O···O bond cleavage is homolytic in nature with a spin-up α electron being present in the proximal oxygen and a spin-down β electron leaving with the distal oxygen atom. This leads to the formation of a Ni^{II}–O$^{\bullet}$ (**3a**) or a Ni^{III}=O (**3b**) species. Formation of species **3a/3b** from species **2** is found to be endothermic by 32.8 kJ·mol^{-1} (Figure 2); however, from the reactant species **1**, the overall reaction is still exothermic (see Figure 4).

Furthermore, the conversion of **1** to **2** requires the loss of a proton; in presence of the highly-basic TMG$_3$tren ligand, it is highly probable that one of the guanidine arms acts as the proton acceptor. The protonated guanidine arm presumably provides additional stabilization to the Ni^{III}=O core, via a stabilizing hydrogen-bonding interaction (see Figure 5), as has been demonstrated in the previous stabilization of an otherwise unstable Fe^{III}–O species by secondary hydrogen-bonding interaction with the ligand.[24c] Furthermore, such hydrogen-bonding interaction of the bound proton with the proximal oxygen atom of the acylperoxo complex **2**, will further reduce the O···O bond cleavage barrier (see Figure 5); these will make the conversion of **2** to **3** exothermic and thermodynamically feasible, as has been observed experimentally. Although, for simplicity, the role of protons has not been considered in the calculation, the influence of protons in the O···O cleavage step as well as in the stabilization of late transition metal-oxo cores are well documented in the literature.[24c-d]

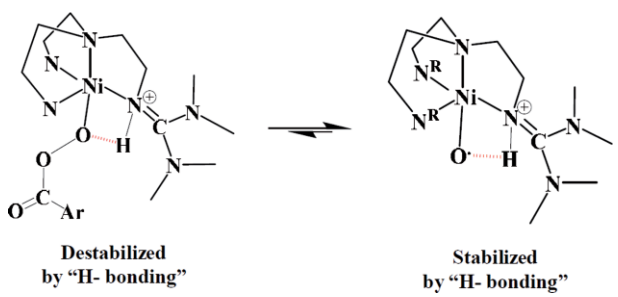

Figure 5. Schematic diagram illustrating the possible of role of proton in the O···O bond cleavage step.

In contrast, the formation of the heterolysis product Ni^{IV}=O (species **4**) is found to be endothermic from species **2** by 13.2 kJ·mol^{-1}. Also, as transition state corresponding to heterolytic cleavage could not be obtained, the kinetic barrier associated with this cleavage has not been estimated.. Furthermore, the homolytic cleavage is predicted to be exothermic with a very small kinetic barrier; thus our calculations favor homolytic cleavage of the O···O bond. [15] The oxo-wall theory suggests that NiIV=O species, which would result from O...O heterolysis, could not exist as the π-bonding orbitals are destabilized. Although this is strictly valid only for octahedral complexes, energetic preference for the formation of Ni^{III}=O over Ni^{IV}=O suggests that, such π bonding are destabilized also in a trigonal bipyramidal arrangement. In the next section, we discuss first the electronic structure of species **3a**, **3b** and **4** and its spectral features before we turn to discuss its reactivity.

Electronic Structure and Spin State Energetics of Species 3a and 3b

It was proposed that these species have the ability to perform hydrogen atom abstraction and oxo-transfer reactions.[20] As these species are highly reactive and transient, there are only indirect spectral evidences for its formation.[20] Species **3a** and **3b** are electromeric species with a variation only in the nature of electrons present in the oxygen atom. A very strong double bond between Ni and O yields species **3b**, whereas only a sigma bond yields species **3a**. For **3a**, since both Ni^{II} and oxygen atoms possess unpaired electrons, there is a possibility of spin-coupling (ferro or antiferro) leading to S = 3/2 or S = 1/2 states with the nature of coupling deciding the ground state structure. Additional electronic complexity also arises for **3a** where the central Ni^{II} ion could also be low-spin. All these possible electronic states for species **3a** and **3b** are shown in Table 1. For species **3b**, the central NiIII ion has two possible spin states S = 3/2 and S = 1/2, as shown in Table 1..

We have computed all possible electronic states for **3a** (^{4}**3a**$_{hs}$, ^{2}**3a**$_{hs}$, ^{2}**3a**$_{ls}$) and our calculations reveal that the ground state of this species is S = 3/2 ^{4}**3a**$_{hs}$ (see Table 1). This is rather expected as the unpaired electrons in the Ni^{II} e$_g$-like orbitals are orthogonal to the π* orbital of the oxyl radical leading to a ferromagnetic coupling and hence a S = 3/2 ground state. The ^{2}**3a**$_{hs}$, ^{2}**3a**$_{ls}$ states are found to be 56.7 kJ·mol^{-1} and 61.3 kJ·mol^{-1} higher in energy, respectively (see Table 1). A very large gap between the ^{4}**3a**$_{hs}$ and ^{2}**3a**$_{hs}$ states reveals that the ferromagnetic coupling between the Ni^{II} and the oxyl radical is very strong: a *J* value of 1415 cm^{-1} is estimated in our calculation for the ^{4}**3a**$_{hs}$ species. This value is rather large; however, given the fact that this is a direct coupling between the radical and a central metal atom, this is within the expected range.[26] The optimized structure, along with the spin density plots for these species are shown in Figure 6 (for the optimized structure of species ^{2}**3a**$_{hs}$ and ^{2}**3a**$_{ls}$ species see Figure S5, Supporting Information).

In ^{4}**3a**$_{hs}$ species, the Ni–O bond length is found to be 1.844 Å, which is shorter than that found in complex **2**, and suggests a single bond between Ni^{II} and O radical. Notably, on the doublet surface the Ni–O bond shrinks significantly; Ni–O bond lengths of 1.751 Å and 1.710 Å have been determined for ^{2}**3a**$_{hs}$ and ^{2}**3a**$_{ls}$, respectively. This reveals that at the doublet surface the Ni–O bond strength enhances significantly. The angle N$_{ax}$–Ni–O increases from 171° to 175° as we go

Table 1. Different spin states possible for species **3a** and **3b** along with the calculated spin density values on Ni and O atoms and their relative energy.

Spin States	Electronic Configurations Ni(II/III)	O•/O	Mulliken spin density		Relative energy [kJ mol^{-1}]
			Ni	O	
^{4}**3a**$_{hs}$	$\pi^*_{yz}{}^{\uparrow\downarrow}\,\pi^*_{xz}{}^{\uparrow\downarrow}\,\delta_{xy}{}^{\uparrow\downarrow}\,\delta_{x^2-y^2}{}^{2\uparrow}\,\sigma^*_{z^2}{}^{2\uparrow}$	$\varphi_O{}^{\uparrow}$	1.586	1.134	0.0
^{2}**3a**$_{hs}$	$\pi^*_{yz}{}^{\uparrow\downarrow}\,\pi^*_{xz}{}^{\uparrow\downarrow}\,\delta_{xy}{}^{\uparrow\downarrow}\,\delta_{x^2-y^2}{}^{2\uparrow}\,\sigma^*_{z^2}{}^{2\uparrow}$	$\varphi_O{}^{\downarrow}$	1.215	-0.366	61.3
^{2}**3a**$_{ls}$	$\pi^*_{yz}{}^{\uparrow\downarrow}\,\pi^*_{xz}{}^{\uparrow\downarrow}\,\delta_{xy}{}^{\uparrow\downarrow}\,\delta_{x^2-y^2}{}^{2\uparrow\downarrow}\,\sigma^*_{z^2}{}^{2}$	$\varphi_O{}^{\uparrow}$	0.128	0.821	56.7
^{4}**3b**$_{hs}$	$\pi^*_{yz}{}^{\uparrow\downarrow}\,\pi^*_{xz}{}^{\uparrow\downarrow}\,\delta_{xy}{}^{\uparrow}\,\delta_{x^2-y^2}{}^{2\uparrow}\,\sigma^*_{z^2}{}^{2\uparrow}$	φ_O	1.524	1.159	3.5
^{2}**3b**$_{ls}$	$\pi^*_{yz}{}^{\uparrow\downarrow}\,\pi^*_{xz}{}^{\uparrow\downarrow}\,\delta_{xy}{}^{\uparrow\downarrow}\,\delta_{x^2-y^2}{}^{2\uparrow}\,\sigma^*_{z^2}{}^{2}$	φ_O	0.133	0.823	41.1

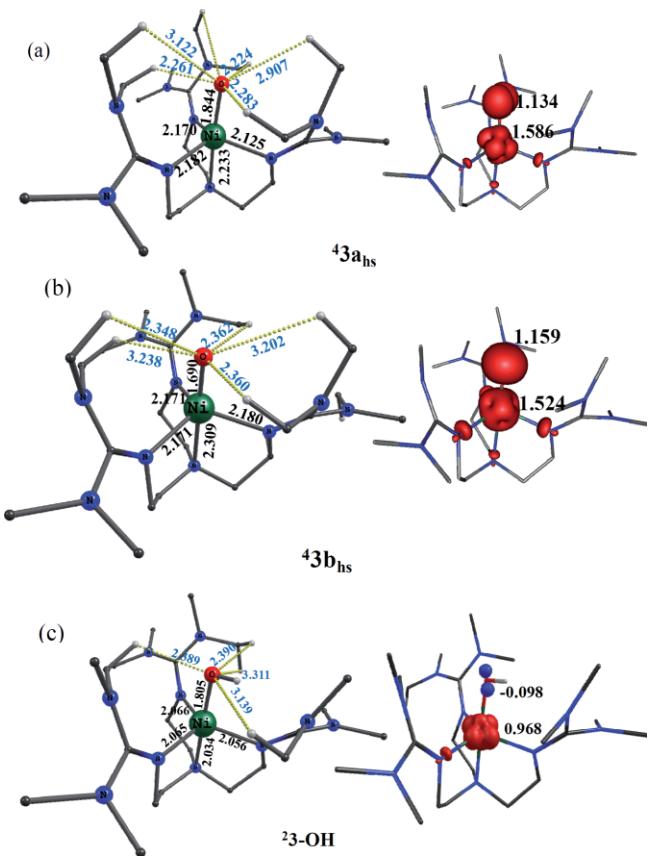

Figure 6. B3LYP optimized structures and spin density plots of the ground state of complex **3a** (a) ^{4}**3a**$_{hs}$; (Ni^{II}–O$^{\bullet}$); (b) complex **3b**: ^{4}**3b**$_{hs}$ (Ni^{III}= O); (c) ^{2}**3**-OH.

from ^{3}**2** to ^{4}**3a**$_{hs}$. The energy level diagram with the computed DFT based orbital for the ^{4}**3a**$_{hs}$ species is shown in Figure 7. The degeneracy in the d_{xy} and $d_{x^2-y^2}$ orbital is lifted significantly due to angular distortions in the equatorial plane and weak interaction of these orbitals with the oxyl radicals. The near degeneracy of the d_{xy} and $d_{x^2-y^2}$ is likely to lead to a very large zero-field splitting as shown by us earlier.[22]

The spin densities on the Ni and oxygen atoms in ^{4}**3a**$_{hs}$ are estimated to be 1.586 and 1.134, respectively. This confirms the presence of a strong radical character at the central oxygen atom. Clearly the Ni^{II} ion undergoes a spin delocalization, while the oxygen atom exhibits a strong spin polarization.

For species **3b**, where a formal Ni^{III}=O is assumed, the Ni–O distances are significantly shorter (Ni–O distance is found to 1.690 Å, see Figure 6b). Here, as well, ^{4}**3b** is found to the ground state and this species is only 3.5 kJ·mol^{-1} higher in energy than the ^{4}**3a** species. Although this species is 3.5 kJ·mol^{-1} higher in energy, this is within the limits of the method and hence one can expect both ^{4}**3a** and ^{4}**3b** to be degenerate. The S = 1/2 state of Ni^{III}=O (^{2}**3b**) is found to lie 14.2 kJ·mol^{-1} higher in energy.

Further NBO analysis [27] reveals that the Ni–O σ bond is more covalent in ^{4}**3b** compared to ^{4}**3a**$_{hs}$. For ^{4}**3a**$_{hs}$ the Ni–O σ-bonding interaction is composed of 16.9 % of Ni(d_{z^2}) and 83.0 % of O(p_z) orbitals (see Figure S9, Supporting Information) and the Wiberg Bond Index (WBI) is estimated to be 0.576 revealing only a single σ bond between the nickel and oxygen atoms. For species ^{4}**3b**, on the other hand, the Ni–O σ-bonding interaction is composed of 32.9 % of Ni(d_{z^2}) and 67.0 % of O(p_z) orbitals with the WBI estimated to be 0.954 (see Figure S9, Supporting Information) revealing clearly the formation of a π bond between the nickel and oxygen atoms. Besides the Ni–O σ bond is found to be more covalent for ^{4}**3b** compared to ^{4}**3a**.

As ^{4}**3a** and ^{4}**3b** are nearly degenerate, one can expect an equilibrium between these two species. The orbital ordering reveals the near degeneracy of π^*_{xz} and π^*_{yz} orbitals for both **3a** and **3b** species. This near degeneracy leads to very small $\pi^*_{xz} \rightarrow \pi^*_{yz}$ transition energies and therefore one can expect a large axial zero-field splitting (zfs) parameter D for both the species. To estimate the axial zfs parameter D and rhombic zfs parameter E, state-average ab initio CASSCF calculations were performed for both **3a** and **3b** using ground state geometries (see computational details for a detailed discussion of the methodology employed). Calculations yield D (E) values of

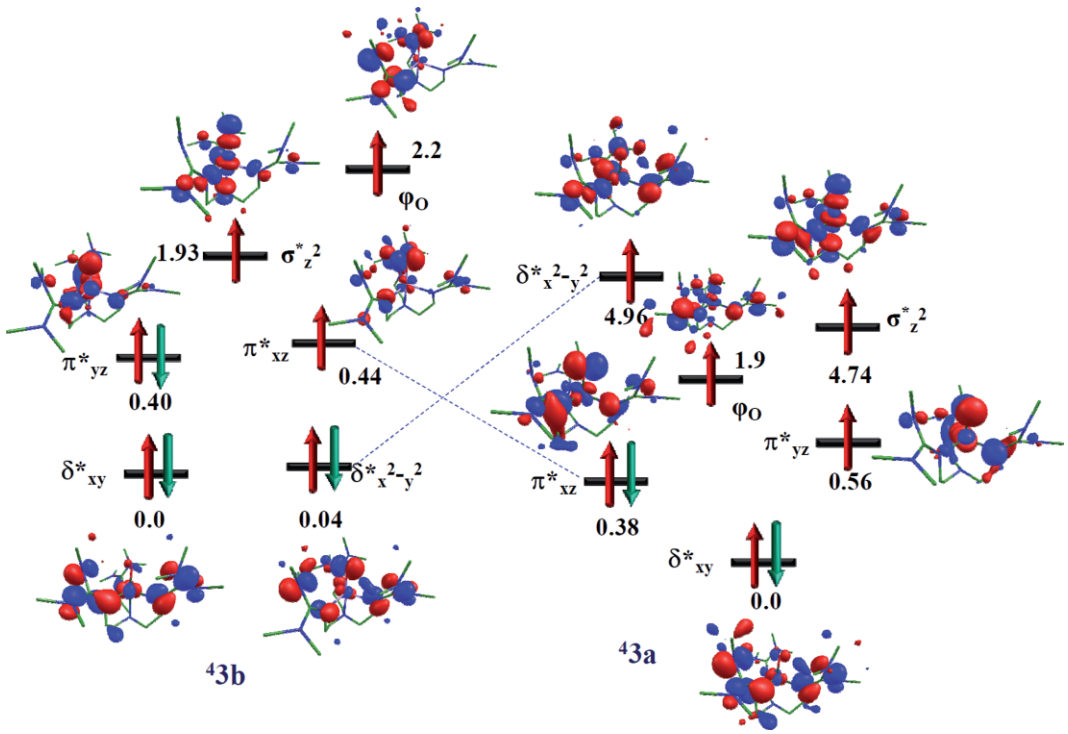

Figure 7. B3LYP computed Eigen-value plot along with energies computed for d-based orbitals for **^{4}3a** and **^{4}3b** species.

–143.9 cm^{-1} (6.4 cm^{-1}) and –201.1 cm^{-1} (0.067 cm^{-1}) for **3a** and **3b**, respectively (see Table S7, Supporting Information). These estimated D values are some of the highest values reported for Ni complexes and this is consistent with the experimentally observed TBP geometry. With such a large D value, only lower $M_s = \pm 3/2$ Kramer's doublet is expected to yield a signal at X-band EPR, and these may attribute to the observed doublet transitions in the experiments.[20] It is important to note here that the main difference between these two species is attributed to the difference in the Ni–O bond length with **^{4}3a** possessing a bond length of 1.844 Å and **^{4}3b** possessing a bond length of 1.690 Å. This difference suggests a possibility of bond-stretch isomerism between these two electromeric form and this has been witnessed earlier in various metal complexes.[28]

To further probe the other spectral features, TDDFT calculations were performed on **^{4}3a**/**^{4}3b** species (see Figures S10 and S11, Supporting Information). Experimentally three peaks were observed at 464 nm, 520 nm, and 794 nm for the proposed Ni^{III}-O/OH species; notably similar features at this region have also been reported previously for the terminal-oxo complexes of the Fe and Co metal ions involving the TMG_3tren ligand system. For **^{4}3a** species, five intense features are observed at 327, 347, 443, 574, and 726 nm (Figure S10, Supporting Information). Features observed at 327, 347 and 443 nm correspond to ligand-to-metal charge transfer (LMCT) transitions. The peak at 574 nm is due to $\delta(d_{xy}–Op_y)^*$ orbitals to the $\sigma^*(Md_{xz}–Op_x)$ antibonding orbitals, whereas the feature observed at 726 nm can be attributed to $\pi(Md_{yz}–Op_y)$ orbital to the $\pi^*(Md_{xy}–Op_x)$ antibonding orbitals.

For **^{4}3b** species, our calculations yield four intense features at 356, 400, 490, and 793 nm, in agreement with the experiments. Features observed at 793 nm correspond to the transitions from the $\delta(d_{xy}–Op_y)^*$ bonding orbitals to the antibonding $\sigma^*(Md_{z^2}–Op_z)$ orbitals, whereas the feature observed at 490 nm can be attributed to the transition from the $\pi(Md_{xz}–Op_x)$ orbital to the $\pi^*(Md_{xz}–Op_x)$ antibonding orbitals. Very intense features observed at 400 nm and 356 nm, respectively, are due to the ligand to metal charge transfer (LMCT) transitions occurring between the ligand and the antibonding π*(Ni–O) orbitals. Experimentally only one broad feature centered around 520 nm is noted and this is broadly in agreement with the computed results.

We have also optimized the hydroxo complex, $[(TMG_3tren)Ni^{III}\text{-}OH]^{+2}$ (complex **3-OH**). It was proposed that the ligand undergoes a self-decay process and transfers a "H" atom to the oxygen atom of the oxo group. Two spin states are possible for complex **3-OH**, S = 3/2 and S = 1/2. Our calculations reveal S = 1/2 as the ground state with the S = 3/2 higher in energy by ca. 20 kJ·mol^{-1}. The optimized structure along with spin density plot of the doublet ground state is given in Figure 6c. The Ni–O(H) and $Ni–N_{ax}$ bond lengths are observed to be 1.863 Å and 2.210 Å respectively. In contrast to the complex **3a/3b**, here the Ni–O bond length is longer and $Ni–N_{ax}$ distances are slightly shorter. This can be attributed to the lack of strong π bonds between the hydroxo and central Ni atoms.

We have also optimized the Ni^{IV}=O species **4** considering S = 2, S = 1, and S = 0 spin states. Here S = 1 (**^{3}4**) is found to be the ground state with the S = 2 and S = 0 states being 18.4 and 97.6 kJ·mol^{-1} higher in energy. The optimized structure

along with the spin density plot of ^{3}**4** species is shown in Figure 8. Here the Ni–O bond length is estimated as 1.785 Å with a longer bond length in S = 2 and a nearly similar bond length in the S = 0 state (see Table S2, Supporting Information). NBO analysis clearly reveal absence of π bond between the Ni and oxygen atoms and WBI index (0.9016) also support a single bond between Ni and oxo suggesting that this species rather exist as Ni^{III}–$O^{\bullet}$ species without the formal double bond, comprising 26.3 % of Ni(d_{z^2}) and 73.6 % of O(p_z) orbitals (see Figure S9, Supporting Information). The spin density plot also depicts this picture with a very strong delocalization of spin density to the oxygen atom with only one electron being located at the central Ni atom. Such strong oxyl radical characters suggest a very high reactivity for these species, if made. This suggest that species **4** predominantly exist as Ni^{III}–$O^{\bullet}$, whereas species **3** likely exist as a combination of Ni^{II}–$O^{\bullet}$ and Ni^{III}=O species.

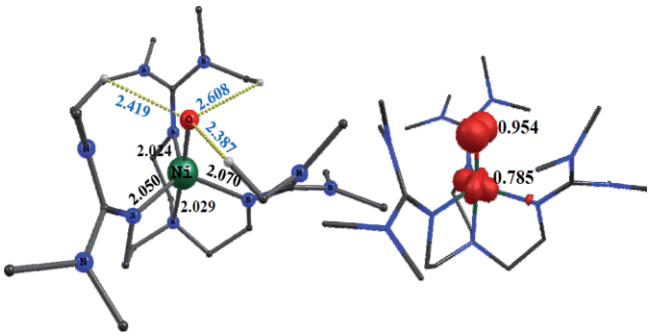

Figure 8. B3LYP optimized structures and spin density plots of the ground state of the complex ^{3}**4**.

Reactivity of Species 3: Towards Establishing the Self-Decay Mechanism of the Ni-Oxo Species

In species **3**, the trigonal bipyramidal arrangement is enforced by the sterically bulky tetramethylguanidinyl donors of the tetradentatetripodal TMG_3tren ligand. The close proximity of the methyl substituents to the oxo-nickel unit facilitates the self-decay of the ligand by intramolecular hydrogen atom abstraction and leads to the formation of a ligand hydroxylated Ni^{II} product. This has been witnessed in the experimental report.[13] A detailed mechanism adapted for our calculations is shown in Scheme 1 and the developed potential energy surface is shown in Figure 9. As mentioned earlier, the oxygen atom of **3** has three strong C–H···O interactions with one of the C–H···O bonds being very strong with a H···O distance of 2.224 Å. [44]

This is in fact the starting point of the mechanism, where this hydrogen atom in closer proximity is expected to be activated by the oxo group leading to the formation of the Ni^{II}-OH species via **ts2**. The barrier heights are estimated to be

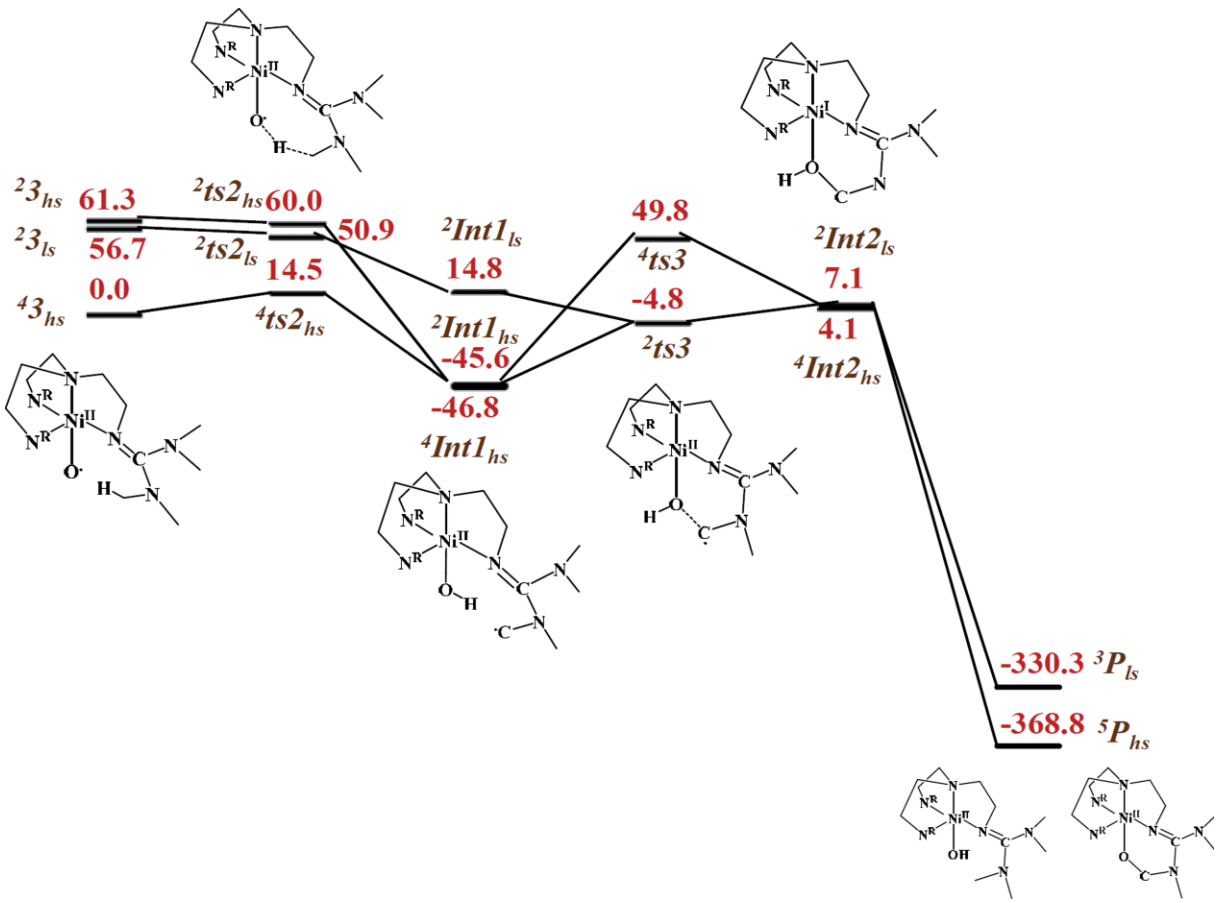

Figure 9. B3LYP computed energy profile diagram for the formation of product from complex **3**.

14.8, 50.9, and 60.0 kJ·mol^{-1} at ^{4}**ts2**$_{hs}$, ^{2}**ts2**$_{hs}$ *and* ^{2}**ts2**$_{ls}$ surfaces, respectively. The optimized structure of the ^{4}**ts2**$_{hs}$ surface is shown in Figure 10. In ^{4}**ts2**$_{hs}$ structure, the newly forming H(1)···O bond length is shortened to 1.241 Å revealing that at the transition state, the hydrogen atom is midway between the oxygen and the carbon atoms. Also, the Ni–O bond length is found to increase from 1.868Å to 1.917 Å. The calculated O–H(1)–C(1) bond angle is nearly linear (162.9°). The computed spin density plot reveals the generation of a significant radical character at the carbon atom (0.405) with the concomitant reduction in the spin density at the oxo atom (from 1.134 to 0.731) and the development of a very small spin density at the hydrogen atom. This reveals that the β electron from the C–H bond has already been transferred to the oxo group leading to the reduction of its spin density at the transition state.

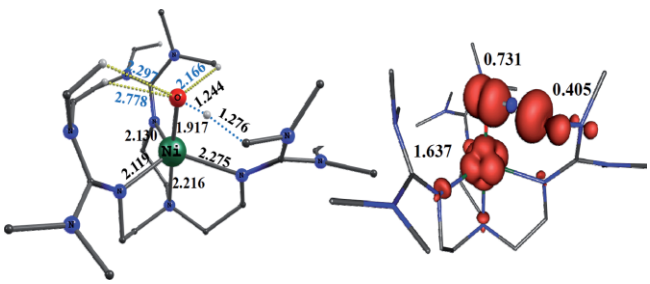

Figure 10. B3LYP optimized structures and spin density plot of the ground state of ^{4}**ts2**$_{hs}$.

The complete transfer of hydrogen atom from C to O leads to the formation of a ligand based radical (**Int1**) and this formation is found to be exothermic (–46.8 kJ·mol^{-1}). The optimized structure and spin density plot of **Int1** is shown in Figure 11. In **Int1** the O–H distance is decreased from 1.241 to 0.971 Å. At this intermediate, the C(1) carbon develops a full radical character (spin density value of 0.850). The spin density at the central Ni atom is estimated to be 1.637 and this is nearly unaltered during the course of the reaction; this suggests that the hydrogen atom abstraction is primarily carried out at the oxo center.

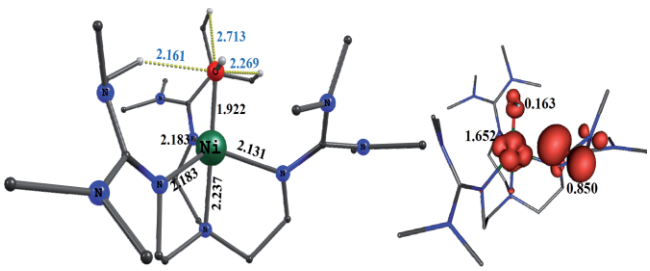

Figure 11. B3LYP optimized structures and spin density plot of the ground state of ^{4}**Int1**$_{hs}$.

For **Int1**, three different spin states are computed with ^{4}**Int1**$_{hs}$ being the ground state and the ^{2}**Int1**$_{hs}$, ^{2}**Int1**$_{ls}$ states lying higher in energy by 1.1 and 14.4 kJ·mol^{-1}, respectively. In the next step, rebound of –OH group to the radical carbon centre is expected to proceed via **ts3**. At the quartet surface the barrier is estimated to be 96.6 kJ·mol^{-1}, while at the doublet surface the barrier is calculated to be 40.8 kJ·mol^{-1}. Although the barrier heights seem significant, the formation of **int1** species is exothermic and this ease out the kinetic barrier. From the reactant energy this step is essentially a barrier-less process leading to the final product.

The optimized structure and spin density plot of **ts3** is shown in Figure 12. In ^{2}**ts3** the O–C(1) distance decreases from 3.138 to 1.935 Å. At the same time the Ni–O bond length increases from 1.922 to 2.017 Å. The Ni–O–C(1) angle is found to be 103.8°. The spin density on Ni is maintained at 1.651. In the next step, the formation of the hydroxylated ligand complex **Int2** is assumed. The formation of this species is found to be endothermic by 50.2 kJ·mol^{-1} from **int1**. Here a quartet state is found to be the ground state with the doublet found to be 3 kJ·mol^{-1} higher in energy. The Ni–O distance at the quartet state increases from 2.017 to 2.011 Å and the O–C(1) distance decreases from 1.935 to 1.384 Å. In the next step, the **Int2** either dimerizes or reacts with **3** to form the hydroxonickel(II)(**Pro1**) and alkoxonickel(II) complex (**Pro2**). The optimized structures and the spin density plots of both the species are shown in Figure 13. The formation of this final product is found to be extremely exothermic by more than 300 kJ·mol^{-1}, revealing a facile reaction once the hydrogen atom abstraction takes place (see Figure 13). The calculated Ni–O bond lengths in the hydroxonickel(II)(**Pro1**) and alkoxonickel(II) complexes (**Pro2**) are found to be 1.913 and 1.968 Å, respectively and this reveals slighter longer Ni–O bond compared to the Ni^{III}-OH complex (**3-OH**). The spin density values on Ni in **Pro1** and **Pro2** confirm the presence of two unpaired electrons on the nickel ion, with some delocalization to other atoms.

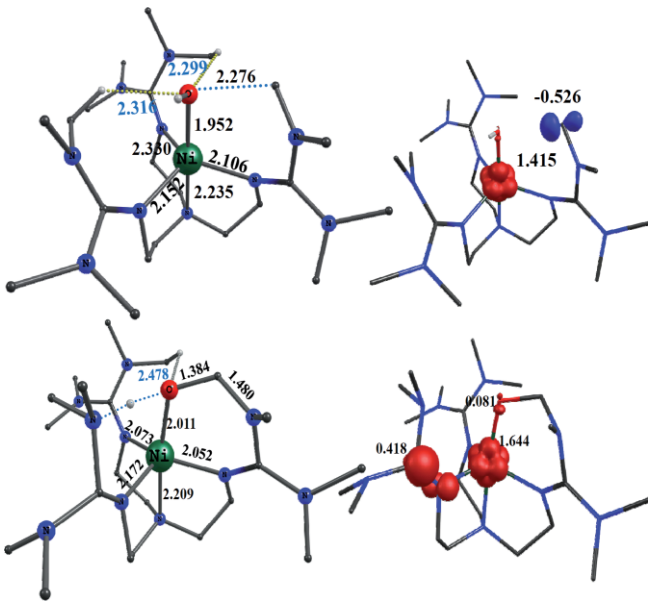

Figure 12. B3LYP optimized structures and spin density plot of the ground state of ^{2}**ts3** (above) and ^{4}**Int2**$_{hs}$ (below).

Intermolecular C–H Bond Activation by the Ni-Oxo Species

After a detailed reactivity study of complex **3** towards intramolecular C–H activation (or ligand self-decay process), we

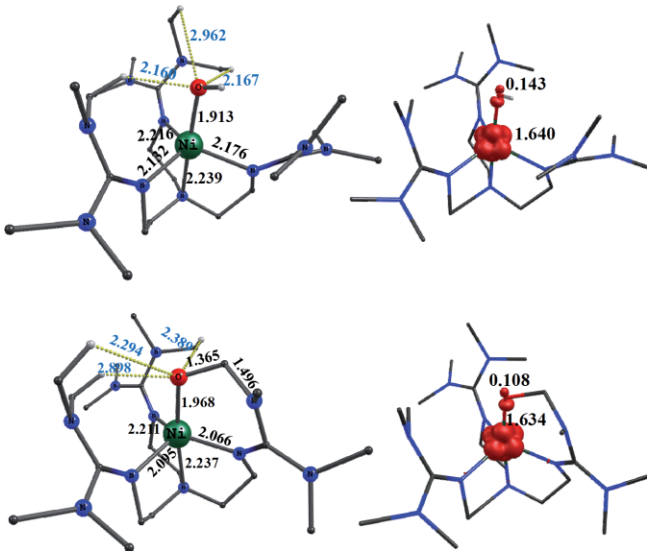

Figure 13. B3LYP optimized structures and spin density plot of the ground state of products **Pro1** (above) and **Pro2** (below).

have further explored the reactivity of the same complex towards the intermolecular C–H activation reaction, to put some more light into the nature of the Ni^{II}–$O^{\bullet}$ species. For this particular study, we have chosen the 9,10-dihydroanthracene molecule (DHA) as our substrate. The optimized structures and the spin density plots of the transition state ($\mathbf{ts_{inter}}$) are shown in Figure 14.

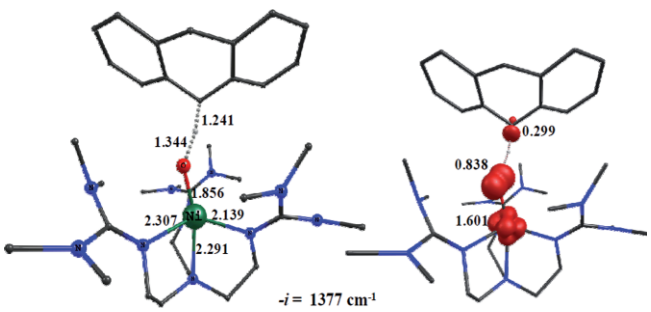

Figure 14. Optimized structure for the ground state of the intermolecular C–H bond activation transition state ($^{4}\mathbf{ts_{inter}}$).

The optimized structure of the ground state shows a shorter Ni–O distance (1.889 Å) compared to the Ni–O distance observed in case of intramolecular ts. The O–H and H–C bond lengths are found to be 1.384 and 1.214 Å, respectively. The spin density plot clearly shows that the radical pathway is superintended for the mechanism to proceed. The O–H–C bond angle is found to be nearly 170°, which is larger than what was found in $^{4}\mathbf{ts2_{hs}}$ (i.e. $\mathbf{ts_{intra}}$). From the shape of the orbital one can predict the involvement of the e_g set of orbitals in nickel and *p* orbital of oxygen in the transition state. The HOMO of the $\mathbf{ts_{inter}}$ and $\mathbf{ts_{intra}}$ are shown in Figure S20 (Supporting Information). The representation of the HOMO orbital of the $\mathbf{ts_{inter}}$ clearly shows involvement of the $\pi^*(Nid_{z^2}–Op_z)$ orbitals and p orbitals of the carbon atom, while in case of the $\mathbf{ts_{intra}}$, the $\pi^*(Nid_{xz}–Op_x)$ orbitals and p orbitals of the carbon atom are involved.

It can be concluded that one transition state is going through a σ pathway ($\mathbf{ts_{inter}}$), whereas the other transition state proceeds through a π pathway ($\mathbf{ts_{intra}}$). The calculated barrier height for the $\mathbf{ts_{inter}}$ is found to be 91.7 kJ·mol^{-1}, which is estimated to be six times larger than what has been observed for the $\mathbf{ts_{intra}}$ (see Figure 15). It confirms that the unique ligand architecture makes intramolecular C–H activation more feasible in contrast to the intermolecular C–H activation step, which requires a huge barrier. Our findings are in agreement with the experimental results that shows generation of **3a/3b** or **3-OH** in only 15 % yield.

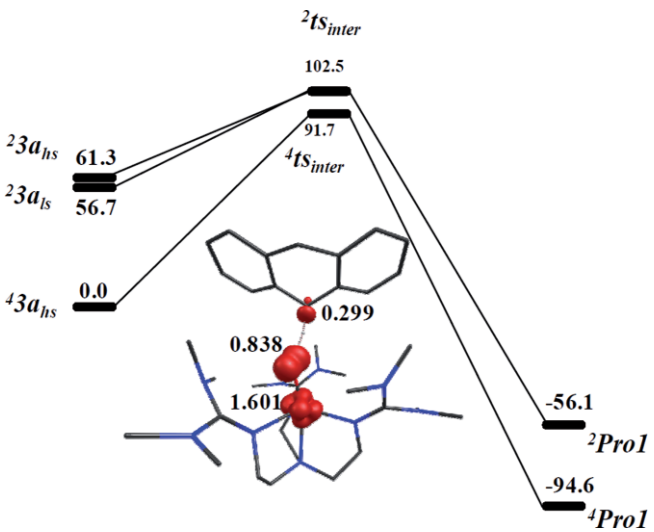

Figure 15. B3LYP computed energy profile diagram for the intermolecular C–H bond activation reaction mediated by complex **3**.

Conclusions

In the present study, we report for the first time theoretical studies on a very rare terminal Ni-oxo species where its generation, spectral features and reactivity pattern are analyzed. The major conclusions derived from this work are summarized below:

(i) Our calculations reveal that the acylperoxonickel(II) intermediate cleaves homolytically with a barrier height of 68 kJ·mol^{-1} from the acylperoxonickel(II) intermediate at the triplet surface leading to the formation of the putative Ni^{III}=O species. On the other hand, the heterolytic cleavage of O···O bond is found to be thermodynamically not favored vis-a-vis homolysis.

(ii) Electronic structure analysis reveal various possible spin-states/electromers for the putative Ni^{III}=O species. Our calculations reveal that the Ni^{II}–$O^{\bullet}$ species, which is an electromeric form of Ni^{III}=O is nearly degenerate in energy with both the species possessing S = 3/2 ground state. As the arrangement around the central Ni atom is trigonaly bipyramidal, the crystal field interaction is not strong enough to force pairing of electrons. Calculations reveal significant radical character for the oxo atom and this could be the driving force behind its agressive oxidative abilities towards C–H bonds. The main difference between the Ni^{II}–$O^{\bullet}$ and Ni^{III}=O is the difference in

the Ni–O distance and the possibility of these two species being bond stretch isomers is proposed. Additionally, ab initio calculations predict extremely large negative zero-field splitting parameter for both the species and this arise due to quasi degenerate $d_{xy}/d_{x^2-y^2}$ orbitals at the central Ni atom.

(iii) The heterolytic cleavage product, the putative Ni^{IV}=O species, however, was found to exist soley as Ni^{III}–$O^{\bullet}$ with a significant radical character at the oxygen atom.

(iv) Both intramolecular and intermolecular C–H bond activation reactions are tested, where the Ni^{II}–$O^{\bullet}$ was found to easily undergo ligand self-decay process as suggested by the experiments. The intermolecular C–H bond activation by DHA substrate was found to be proceeded through radical mechanism with a moderate barrier for the hydrogen abstraction step.

To this end, our theoretical study suggests a possible reactivity for the Ni-Oxo species beyond a two-state-reactivity concept (see[25], reference therein), where two electromeric forms (or bond-stretch isomers) are also potentially involved in the reactivity, invoking a two-state-two-isomers-reactivity. The scope for such examples are likely to extend beyond the example studied here.

Methodology

All the calculations were carried out using the Gaussian 09 suite of program.[29] The geometry optimizations were performed with B3LYP functional.[30] The B3LYP has a proven track record of predicting the structures and the energetics accurately for such metal mediated catalytic reactions. LACVP basis set comprising LanL2DZ – Los Alamos effective core potential for Ni[31] and a 6-31G* basis set for the C, H, N, S, F, Cl, O atoms[32] was employed for geometry optimization and the optimized geometries were used to perform single point energy calculations using a TZVP basis set on all atoms. The solvation energies were computed using PCM solvation model[33] employing dichloromethane as the solvent. Frequency calculations were performed on the optimized structures to verify that they are minima on the potential-energy surface (PES) and also to obtain free energy corrections. The quoted DFT energies are B3LYP solvation energies incorporating Gibbs free energies correction at computed at the temperature of 298.15 K, unless otherwise mentioned. The fragment approach available in Gaussian 09 was employed to aid smooth convergence in case of radical intermediates. The ORCA package[34] was used to calculate the UV/Vis spectra and other spin Hamiltonian parameters (g and D tensors). B3LYP exchange correlation functionals[30] were used along with the TZVP basis set on the Gaussian optimized geometries to compute the spectral parameters. Time dependent density functional theory (TDDFT) implemented in the ORCA program was used for the calculation of excitation energies. To calculate single-ion anisotropies of the $Ni^{II/III}$ centers high-level ab initio calculations were employed. All these calculations were performed using the MOLCAS 8.0 suite of programs.[35] Basis sets describing all the atoms were taken from the ANO-RCC library available in the MOLCAS package. Herein, we employed the [ANO-RCC.6s5p3d2f1g.] basis set for Ni atoms, [ANO-RCC.3s2p1d] basis set for C, N, and O atoms, and [ANO-RCC..2s1p.] basis set for H atoms. High-level ab initio calculations were employed to compute the single-ion anisotropies of the central Ni^{III} atoms. For the Ni^{III} atoms, the active space comprises eight active electrons in five active metal-based d orbitals, that is, a CAS(7,5) setup. We computed 10 quartets and 35 doublets in the CI (Configuration Interaction) procedure, followed by the mixing all of these states in the RASSI-SO module to compute the spin-orbit states. Similarly, these SO states were introduced in the SINGLE_ANISO module[36] to compute the g-tensors for each of the central Ni^{III} atoms.

Supporting Information (see footnote on the first page of this article): Supporting information contains, selected geometrical parameters of all the species computed, optimized geometries, spin density plots, Eigen-value plots, NBO donor-acceptor interactions, simulated absorption spectra, computed spin Hamiltonian parameters, AIM analysis data and the coordinates of all the species computed.

Acknowledgements

GR would like to thank SERB-DST (Grant number EMR/2014/000247) and BP would like to acknowledge IIT Bombay and UGC for funding. K.R. thanks the Heisenberg-Program of DFG for financial support.

Keywords: Density functional calculations; High-valent nickel oxo; Hydroxo; Nickel

References

[1] a) P. A. Frey, A. D. Hegeman, *Enzymatic Reaction Mechanisms*, Oxford University Press, **2007**; b) B. Meunier, *Biomimetic Oxidations Catalyzed by Transition Mmetal Complexes*, World Scientific, **2000**; c) H. Sigel, A. Sigel, *Metal Ions in Biological Systems, Electron Transfer Reactions in Metalloproteins*, vol. 27, CRC Press, **1991**.
[2] a) J. T. Groves, *J. Inorg. Biochem.* **2006**, *100*, 434–447; b) J. T. Groves, Y.-Z. Han, in *Cytochrome P450*, Springer, **1995**, pp. 3–48; c) J. Hohenberger, K. Ray, K. Meyer, *Nat. Commun.* **2012**, *3*, 720.
[3] a) L. E. Grove, T. C. Brunold, *Comments Inorg. Chem.* **2008**, *29*, 134–168; b) R. Holm, *Chem. Rev.* **1987**, *87*, 1401–1449.
[4] a) J. P. Klinman, *Chem. Rev.* **1996**, *96*, 2541–2562; b) E. I. Solomon, U. M. Sundaram, T. E. Machonkin, *Chem. Rev.* **1996**, *96*, 2563–2606.
[5] S. W. Ragsdale, *J. Biol. Chem.* **2009**, *284*, 18571–18575.
[6] a) A. Parkins, *Appl. Organomet. Chem.* **2000**, *14*, 75–76; b) W. Keim, *Angew. Chem. Int. Ed. Engl.* **1990**, *29*, 235–244.
[7] a) P. M. Vignais, B. Billoud, *Chem. Rev.* **2007**, *107*, 4206–4272; b) J. C. Fontecilla-Camps, A. Volbeda, C. Cavazza, Y. Nicolet, *Chem. Rev.* **2007**, *107*, 4273–4303.
[8] a) B. Palenik, B. Brahamsha, F. Larimer, M. Land, L. Hauser, P. Chain, J. Lamerdin, W. Regala, E. Allen, J. McCarren, *Nature* **2003**, *424*, 1037–1042; b) J. Wuerges, J.-W. Lee, Y.-I. Yim, H.-S. Yim, S.-O. Kang, K. D. Carugo, *Proc. Natl. Acad. Sci. USA* **2004**, *101*, 8569–8574; c) H.-D. Youn, E.-J. Kim, J.-H. Roe, Y. C. Hah, S.-O. Kang, *Biochem. J.* **1996**, *318*, 889.
[9] a) R. P. Hausinger, P. A. Karplus, *Urease*, in *Handbook of Metalloproteins* (Eds.: A. Messerschmidt, R. Huber, T. Poulos, K. Wieghardt), John Wiley & Sons: Chichester, UK, **2001**; 2, pp 867– 879; b) R. K. Andrews, R. L. Blakeley; B. Zerner, in *The Bioinorganic Chemistry of Nickel* (Ed.: J. R. Lancaster Jr), VCH Publishers: New York, 1988; pp 141–165.
[10] S. W. Ragsdale, E. Pierce, *Biochim. Biophys. Acta Proteins Proteomics* **2008**, *1784*, 1873–1898.
[11] W. Martin, M. J. Russell, *Philos. Trans. R. Soc. London B; Biol. Sci.* **2007**, *362*, 1887–1926.
[12] a) R. Cammack, in *Advances in Inorganic Chemistry*, vol. 32, Elsevier, **1988**, pp. 297–333; b) J. R. Lancaster, *The Bioinorganic Chemistry of Nickel*, VCH Publisher, New York, **1988**.
[13] T. Corona, A. Company, *Chem. Eur. J.* **2016**, *22*, 13422–13429.

[14] a) S. Yao, M. Driess, *Acc. Chem. Res.* **2011**, *44*, 276–287; b) M. Balamurugan, R. Mayilmurugan, E. Suresh, M. Palaniandavar, *Dalton Trans.* **2011**, *40*, 9413–9424; c) T. Nagataki, Y. Tachi, S. Itoh, *Chem. Commun.* **2006**, 4016–4018.
[15] P. Pirovano, E. R. Farquhar, M. Swart, A. R. McDonald, *J. Am. Chem. Soc.* **2016**, *138*, 14362–14370.
[16] a) K. Shiren, S. Ogo, S. Fujinami, H. Hayashi, M. Suzuki, A. Uehara, Y. Watanabe, Y. Moro-oka, *J. Am. Chem. Soc.* **2000**, *122*, 254–262; b) S. Itoh, H. Bandoh, M. Nakagawa, S. Nagatomo, T. Kitagawa, K. D. Karlin, S. Fukuzumi, *J. Am. Chem. Soc.* **2001**, *123*, 11168–11178; c) R. Schenker, B. S. Mandimutsira, C. G. Riordan, T. C. Brunold, *J. Am. Chem. Soc.* **2002**, *124*, 13842–13855; d) K. Fujita, R. Schenker, W. Gu, T. C. Brunold, S. P. Cramer, C. G. Riordan, *Inorg. Chem.* **2004**, *43*, 3324–3326; e) J. Cho, H. Furutachi, S. Fujinami, M. Suzuki, *Angew. Chem.* **2004**, *116*, 3362–3365.
[17] T. Nagataki, K. Ishii, Y. Tachi, S. Itoh, *Dalton Trans.* **2007**, 1120–1128.
[18] Y. Shiota, K. Yoshizawa, *J. Am. Chem. Soc.* **2000**, *122*, 12317–12326.
[19] a) F. F. Pfaff, S. Kundu, M. Risch, S. Pandian, F. Heims, I. Pryjomska-Ray, P. Haack, R. Metzinger, E. Bill, H. Dau, *Angew. Chem. Int. Ed.* **2011**, *50*, 1711–1715; b) T. Tano, Y. Okubo, A. Kunishita, M. Kubo, H. Sugimoto, N. Fujieda, T. Ogura, S. Itoh, *Inorg. Chem.* **2013**, *52*, 10431–10437; c) D. Maiti, D.-H. Lee, K. Gaoutchenova, C. Würtele, M. C. Holthausen, A. A. Narducci Sarjeant, J. Sundermeyer, S. Schindler, K. D. Karlin, *Angew. Chem. Int. Ed.* **2008**, *47*, 82–85.
[20] F. F. Pfaff, F. Heims, S. Kundu, S. Mebs, K. Ray, *Chem. Commun.* **2012**, *48*, 3730–3732.
[21] S. Hikichi, K. Hanaue, T. Fujimura, H. Okuda, J. Nakazawa, Y. Ohzu, C. Kobayashi, M. Akita, *Dalton Trans.* **2013**, *42*, 3346–3356.
[22] G. A. Craig, A. Sarkar, C. H. Woodall, M. A. Hay, K. E. R. Marriott, K. V. Kamenev, S. A. Moggach, E. K. Brechin, S. Parsons, G. Rajaraman, M. Murrie, *Chem. Sci.* **2018**, *9*, 1551–1559.
[23] J. Nakazawa, S. Terada, M. Yamada, S. Hikichi, *J. Am. Chem. Soc.* **2013**, *135*, 6010–6013.
[24] a) S. Hikichi, C. Kobayashi, M. Yoshizawa, M. Akita, *Chem. Asian J.* **2010**, *5*, 2086–2092; b) X. Zhang, H. Furutachi, T. Tojo, T. Tsugawa, S. Fujinami, T. Sakurai, M. Suzuki, *Chem. Lett.* **2011**, *40*, 515–517; c) C. E. MacBeth, A. P. Golombek, V. G. Young Jr., C. Yang, K. Kuczera, M. P. Hendrich, A. S. Borovik, *Science* **2000**, *289*, 938–941; d) W. Nam, *Acc. Chem. Res.* **2007**, *40*, 465–465 and references cited therein.
[25] a) A. Ansari, A. Kaushik, G. Rajaraman, *J. Am. Chem. Soc.* **2013**, *135*, 4235–4249; b) A. Ansari, G. Rajaraman, *Phys. Chem. Chem. Phys.* **2014**, *16*, 14601–14613.
[26] S. Tewary, I. A. Gass, K. S. Murray, G. Rajaraman, *Eur. J. Inorg. Chem.* **2013**, *2013*, 1024–1032.
[27] E. D. Glendening, K. Badenhoop, A. E. Reed, J. E. Carpenter, J. A. Bohmann, C. M. Morales, F. Weinhold, *NBO 5.0, Theoretical Chemistry Institute, University of Wisconsin, Madison* **2001**.
[28] a) M. Mayer James, *Angew. Chem. Int. Ed.* **2003**, *42*, 286–287; b) S. K. Padamati, D. Angelone, A. Draksharapu, G. Primi, D. J. Martin, M. Tromp, M. Swart, W. R. Browne, *J. Am. Chem. Soc.* **2017**, *139*, 8718–8724; c) Y. Jean, A. Lledos, J. K. Burdett, R. Hoffmann, *J. Am. Chem. Soc.* **1988**, *110*, 4506–4516.
[29] M. J. Frisch, G. W. Trucks, H. B. Schlegel, G. E. Scuseria, M. A. Robb, J. R. Cheeseman, J. A. Montgomery Jr., T. Vreven, K. N. Kudin, J. C. Burant, J. M. Millam, S. S. Iyengar, J. Tomasi, V. Barone, B. Mennucci, M. Cossi, G. Scalmani, N. Rega, G. A. Petersson, H. Nakatsuji, M. Hada, M. Ehara, K. Toyota, R. Fukuda, J. Hasegawa, M. Ishida, T. Nakajima, Y. Honda, O. Kitao, H. Nakai, M. Klene, X. Li, J. E. Knox, H. P. Hratchian, J. B. Cross, V. Bakken, C. Adamo, J. Jaramillo, R. Gomperts, R. E. Stratmann, O. Yazyev, A. J. Austin, R. Cammi, C. Pomelli, J. W. Ochterski, P. Y. Ayala, K. Morokuma, G. A. Voth, P. Salvador, J. J. Dannenberg, V. G. Zakrzewski, S. Dapprich, A. D. Daniels, M. C. Strain, O. Farkas, D. K. Malick, A. D. Rabuck, K. Raghavachari, J. B. Foresman, J. V. Ortiz, Q. Cui, A. G. Baboul, S. Clifford, J. Cioslowski, B. B. Stefanov, G. Liu, A. Liashenko, P. Piskorz, I. Komaromi, R. L. Martin, D. J. Fox, T. Keith, M. A. Al-Laham, C. Y. Peng, A. Nanayakkara, M. Challacombe, P. M. W. Gill, B. Johnson, W. Chen, M. W. Wong, C. Gonzalez, J. A. Pople, et al., *Gaussian, Inc. Wallingford CT* **2009**.
[30] a) C. Lee, W. Yang, R. G. Parr, *Phys. Rev. B* **1988**, *37*, 785–789; b) A. D. Becke, *J. Chem. Phys.* **1993**, *98*, 5648–5652; c) P. Stephens, F. Devlin, C. Chabalowski, M. J. Frisch, *J. Phys. Chem.* **1994**, *98*, 11623–11627.
[31] a) P. J. Hay, W. R. Wadt, *J. Chem. Phys.* **1985**, *82*, 299–310; b) P. J. Hay, W. R. Wadt, *J. Chem. Phys.* **1985**, *82*, 270–283; c) W. R. Wadt, P. J. Hay, *J. Chem. Phys.* **1985**, *82*, 284–298; d) R. Kumar, M. Katari, A. Choudhary, G. Rajaraman, P. Ghosh, *Inorg. Chem.* **2017**, *56*, 14859–14869.
[32] a) R. Ditchfield, W. J. Hehre, J. A. Pople, *J. Chem. Phys.* **1971**, *54*, 724–728; b) W. J. Hehre, L. Radom, P. R. Schleyer, J. A. Pople, Ab initio *Molecular Orbital Theory*, Wiley: New York, **1986**.
[33] a) E. Cances, B. Mennucci, J. Tomasi, *J. Chem. Phys.* **1997**, *107*, 3032–3041; b) M. Cossi, G. Scalmani, N. Rega, V. Barone, *J. Chem. Phys.* **2002**, *117*, 43–54.
[34] F. Neese, *Wiley Interdiscip. Rev. : Comput. Mol. Sci.* **2012**, *2*, 73–78.
[35] F. Aquilante, T. B. Pedersen, V. Veryazov, R. Lindh, *WIREs Comput. Mol. Sci.* **2013**, *3*, 143–149.
[36] a) L. F. Chibotaru, L. Ungur, *J. Chem. Phys.* **2012**, *137*, 064112; b) L. Ungur, L. Chibotaru, *Computational Modelling of the Magnetic Properties of Lanthanide Compounds*, in *Lanthanides and Actinides in Molecular Magnetism*, Wiley-VCH, Weinheim, Germany, **2015**, pp. 153–184.

Received: April 2, 2018
Published online: July 26, 2018

